ACS APPLIED ENERGY MATERIALS

www.acsaem.org Article

Sulfone-Modified Perylene Acceptors with Improved Permittivity for Bilayer Organic Solar Cells Processed from Non-halogenated Solvents

Peter Fürk, Matiss Reinfelds, Ilie Hanzu, Theresa Hartl, Jana B. Schaubeder, Elena Zuccala, Heinz Amenitsch, Thomas Rath,* and Gregor Trimmel*

Cite This: *ACS Appl. Energy Mater.* 2023, 6, 1544−1554 Read Online

ACCESS | Metrics & More | Article Recommendations | Supporting Information

ABSTRACT: Organic photovoltaics show high promise as a technology for sustainable energy conversion. A prominent strategy to reduce the substantial energy loss of organic solar cells is to synthesize high-permittivity (high-ε) active layer materials. However, despite the increase in permittivity, many of the high-ε materials achieved only inferior efficiencies, which is generally explained with a worse bulk heterojunction morphology. In this work, we tackled this issue by preparing high-ε acceptors and incorporating them in a bilayer setup, which we optimized using the systematic Design of Experiment (DoE) approach. The prepared acceptors are based on a perylene-linker-perylene scaffold, to which we attached polar sulfone-containing side chains. The relative permittivity of these acceptors increased by over 50% compared to their alkylated analogues. Simultaneously, some of the acceptors have greatly improved solubilities in non-halogenated "green" solvents. Both improvements enabled us to build bilayer organic solar cells from *o*-xylene and THF with PTQ10 as the donor, while simultaneously increasing the efficiency to 5.51% with a high open-circuit voltage of 1.3 V. Our results show that using a bilayer setup can successfully prevent morphology-related efficiency losses when employing high-ε materials. Combining this approach with a systematic optimization method (DoE) can unlock the theoretical potential of permittivity modification in organic solar cell research.

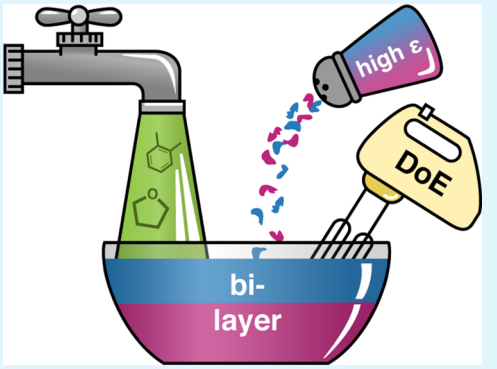

KEYWORDS: *Design of Experiment, bilayer solar cell, permittivity, organic solar cells, dye synthesis, sulfone side chains*

INTRODUCTION

In the last decade, organic solar cells (OSCs) have emerged as a potent technology for sustainable energy conversion. With their attractive features, such as flexible and lightweight design, potential roll-to-roll processing and strong light absorption, global research interest in OCSs has increased constantly.[1−4] With the prominent non-fullerene acceptors, power conversion efficiencies (PCEs) have recently climbed as high as 19.6%.[5,6] To further push PCEs toward their theoretical limit, research groups follow numerous strategies. In 2012, Hummelen *et al.* suggested that increasing the dielectric permittivity of the active layer could significantly improve the OSCs efficiency due to reduced losses during charge generation.[7] The beneficial effects of an increased permittivity have been shown on many important characteristics and processes within the OSCs, such as the exciton binding energy,[8] trap-assisted[9] and bimolecular[10] recombination rates and the reorganization energy upon charge transfer.[11] Because of this wide-ranging impact, permittivity modification in OSCs is a popular field of research.[12] Various strategies to modify the active layer permittivity have emerged, such as adding high-ε additives,[13−15] expanding the conjugated π-system[16] or introducing large, polarizable halogen atoms.[17] Another popular strategy is the introduction of polar side chains to the donor or acceptor molecule, such as oligo ethylene glycol chains or sulfone containing chains.[18−22] This aims to increase the molar polarization P_m of a molecule, which is linked to the relative permittivity ε_r via the Debye equation

$$\frac{\varepsilon_r - 1}{\varepsilon_r + 2} = \frac{\rho}{M} P_m \quad (1)$$

where ρ and M are the mass density and molar mass of the material, respectively. P_m itself increases with both, a higher permanent dipole moment of the molecule or a higher polarizability by external electric fields.[23] This approach has

Received: October 21, 2022
Accepted: January 13, 2023
Published: January 31, 2023

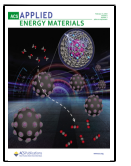

Scheme 1. Structure of the Synthesized Products

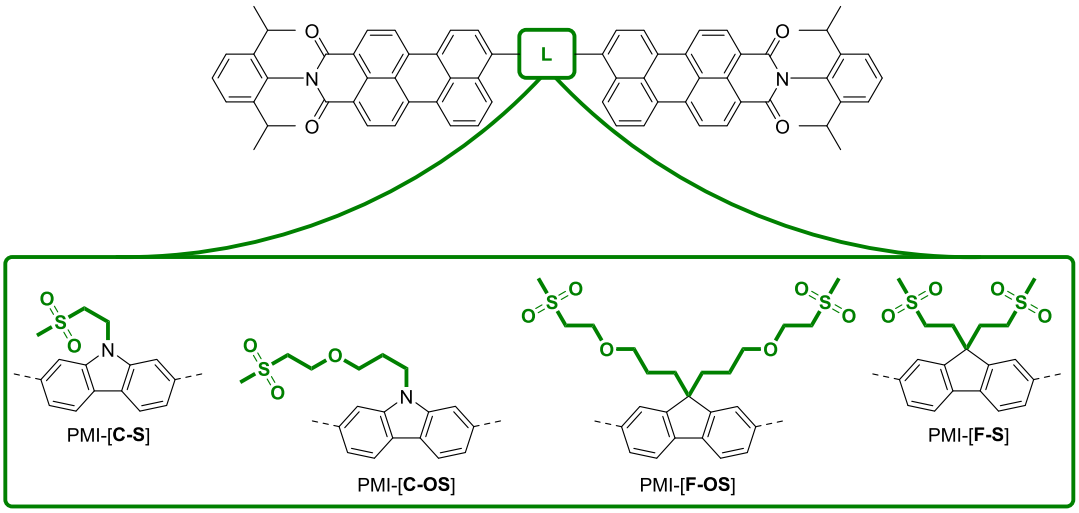

already been tested by our group by the incorporation of diethylene glycol side chains to perylene-linker-perylene acceptors.[24] Although polar side chain engineering is a straightforward and effective method to obtain high-permittivity (high-ε) materials, it usually strongly complicates the subsequent optimization process of the OSC setup. The opposing chemical nature of polar side chains and the overall nonpolar aromatic semiconductors often manifests in a difference in solubility or incompatible surface energies. Therefore, it is challenging to process high-ε acceptors with typical donor polymers. Numerous examples in the literature, including our recent work,[24] report new high-ε acceptors that achieved poorer PCEs than their simple alkylated counterparts.[22,25−27] This behavior is generally explained by a worsening of the donor−acceptor morphology in the complex bulk heterojunction (BHJ).

In this work, we tackled this problem by combining molecular permittivity engineering with a switch to the simpler bilayer OSC setup. We then applied the highly systematic and efficient Design of Experiment (DoE)[28−30] method to the intrinsically complex and multivariate OSCs optimization process. That way, we show a valuable procedure to fully utilize the whole potential of high-ε materials. In recent works,[31,32] we already prepared A-D-A type acceptors comprising perylene monoimide (PMI) as end groups and electron rich donors (fluorene, carbazole, indenofluorene). PMI derivatives have not only a strong UV−Vis absorption and high thermal and photochemical stability but can also be modified easily due to their straightforward synthetic preparation.[33,34] By switching the side chain on the linker to diethylene glycol, we already showed that the permittivity can be improved.[24] Here, we shifted our focus to sulfone-based side chains. The sulfone group was chosen because of its exceptionally high dipole moment (4.5 D)[20] and its strong influence on solubility properties. To add more dipoles and provide higher flexibility,[18] an ether linker was included in the side chain. Because of its ability to rotate more freely than a simple alkyl chain, the ether linker is expected to work as a joint for the sulfone group to reorient easily in an external electric field. Specifically, we introduce four PMI-linker-PMI acceptors PMI-[**F-S**], PMI-[**C-S**], PMI-[**F-OS**], and PMI-[**C-OS**], containing polar sulfone and sulfone-ether side chains on the fluorene and carbazole linkers, respectively (Scheme 1). We then investigate their performance in combination with PTQ10 as donor polymer in a bilayer approach.

RESULTS AND DISCUSSION

Synthesis. To obtain new high-ε acceptors, we incorporated sulfone and ether groups via side chains into PMI-based A-D-A acceptors according to the synthesis scheme (Scheme 2). First, we added the side chains to the fluorene and carbazole linkers, respectively. The methyl-sulfone-ethyl-groups were introduced by a Michael addition reaction starting from methyl vinyl sulfone and deprotonated 2,7-dibromo-carbazol and fluorene, respectively, giving compounds **2** (91%) and **3** (99%) in high yields. The (3-(2-(methylsulfonyl)-ethoxy)propyl) side chain was prepared by oxa-Michael addition of methyl vinyl sulfone and 3-bromopropanol and was then introduced to the linker molecules via nucleophilic substitution to give compounds **4** (38%) and **5** (55%) with moderate yields. Compounds **4** and **5** were subsequently coupled with the PMI-boronic ester derivative (**6c**) in a Suzuki reaction, to obtain the final A-D-A systems PMI-[**F-OS**] and PMI-[**C-OS**]. In the opposite approach, compounds **2** and **3** were converted to the corresponding boronic ester derivative and coupled with the PMI-bromide (**6b**) yielding PMI-[**F-S**] and PMI-[**C-S**]. ^{1}H and ^{13}C NMR spectroscopy and mass spectrometry were used as standard measurements for material characterization. A comprehensive synthetic description is enclosed in the Supporting Information. The solubilities of PMI-[**F-S**] and PMI-[**C-S**] turned out to be too low for OSC applications, explainable by too short side chains for the large aromatic molecules. Therefore, these two molecules were no further considered and a thorough determination of the physical properties was conducted only of PMI-[**F-OS**] and PMI-[**C-OS**] (UV−Vis spectra, see Figure S18c).

Physical Properties. To determine the physical properties of PMI-[**F-OS**] and PMI-[**C-OS**], we conducted UV−Vis absorption and fluorescence spectroscopy, thermal analysis comprising thermogravimetric analysis (TGA) and differential scanning calorimetry (DSC), and permittivity measurements. The results are summarized in Figure 1 and Table 1.

The UV−Vis absorption spectra in $CHCl_3$ (Figure 1a) of both acceptors show a maximum absorption at approx. 530 nm, with a strong absorption coefficient of 8.2−8.5 × 10^4 L mol^{-1} cm^{-1}. Both compounds show an emission at approx. 575

https://doi.org/10.1021/acsaem.2c03433
ACS Appl. Energy Mater. 2023, 6, 1544−1554

Scheme 2. Synthetic Routes to the Targeted Acceptors

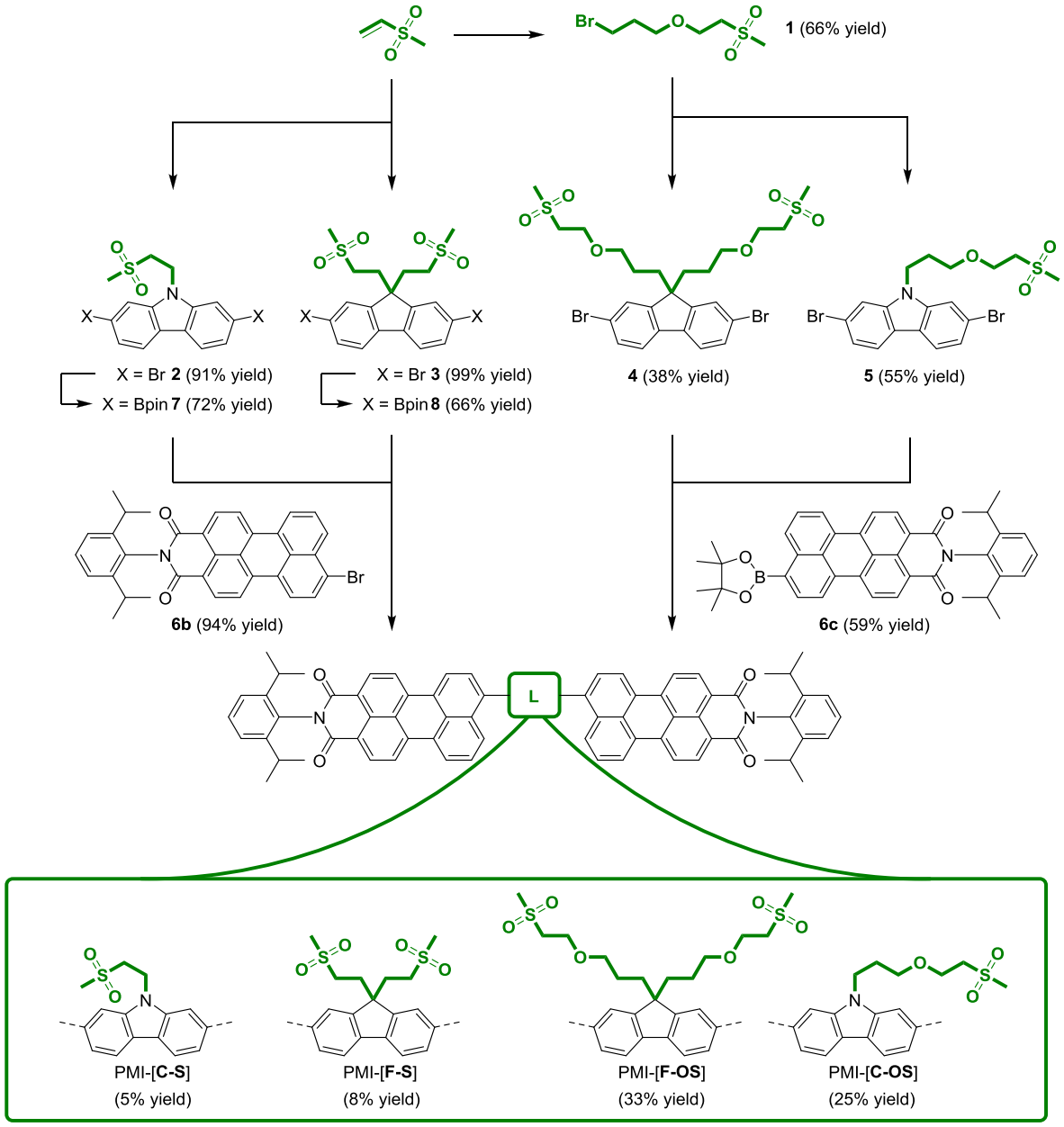

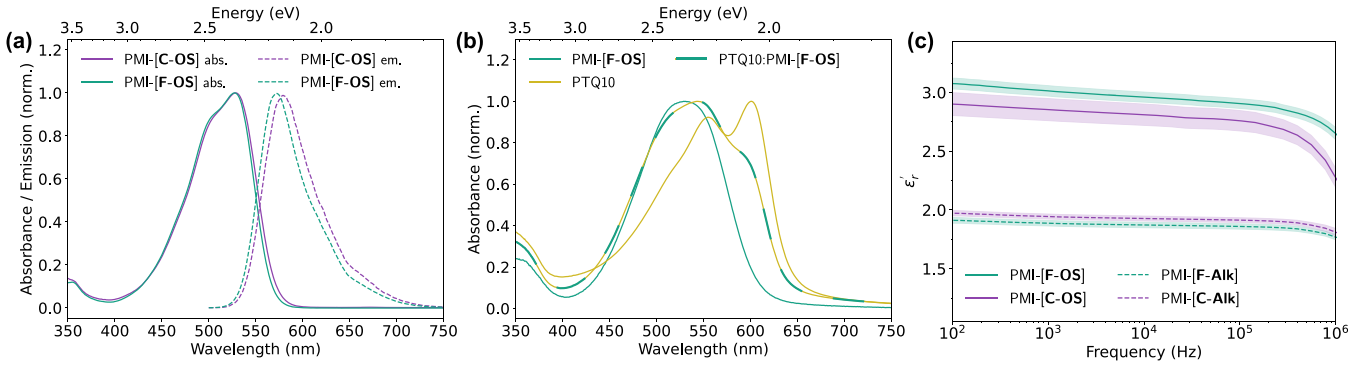

Figure 1. Optical and dielectric properties of PMI-[**F-OS**] and PMI-[**C-OS**]. (a) Normalized UV−Vis absorption (solid) and emission (dashed) spectra in $CHCl_3$ (both at 0.01 mg ml^{-1}, emission excited at 485 nm). (b) Thin film absorbance of PMI-[**F-OS**], PTQ10 and their blend (ratio 1:1 w:w). (c) Relative permittivity ε_r as a function of the electric field frequency of the new (solid) and reference (dashed) compounds (line: arithmetic mean, shaded area: 95% confidence interval, values averaged from 20 to 30 measurements, respectively).

https://doi.org/10.1021/acsaem.2c03433
ACS Appl. Energy Mater. 2023, 6, 1544−1554

Table 1. Physical Characterization of the Acceptors

compound	$\lambda_{max}^{sol.,\,abs.}$ (nm)	$\epsilon_{max}^{sol.}$ (l mol^{-1} cm^{-1})	$\lambda_{max}^{sol.,\,em.}$ (nm)	Φ_{pl} (1)	E_g^{opt}[a] (eV)	E_g^{opt}[b] (eV)	E_{HOMO} (eV)	E_{LUMO} (eV)	E_g^{CV}[c] (eV)	T_g[d] (°C)	ε_r[e] (1)
PMI-[**F-OS**]	527	8.5×10^4	572	0.78	2.24	2.03	−6.10	−4.03	2.07	420	2.90
PMI-[**C-OS**]	529	8.2×10^4	579	0.78	2.25	2.05	−6.07	−4.10	1.97	412	2.76

[a]Optical gap in solution, determined from the intersection of absorbance and emission spectra in $CHCl_3$. [b]Optical gap as thin film, determined from the absorbance spectra of the respective thin film by the tangent method. [c]Band gap of drop-cast films, determined by CV, calcd. from $E_{LUMO} - E_{HOMO}$. [d]Defined as the temperature at 5% weight loss. [e]Relative permittivity at 10^5 Hz.

nm with Stokes shifts of 45 and 50 nm, respectively, and a high fluorescence quantum yield of 78% for both acceptors, indicating that in solution, non-radiative recombination occurs only on a small scale. The optical properties in solution are nearly identical with other PMI-linker-PMI acceptors bearing different side chains.[24,31] The thin film UV−Vis absorption spectrum of PMI-[**F-OS**] (Figure 1b) shows a slight red shifted absorption onset and peak broadening but an almost identical absorption maximum. The TGA measurements (Figure S18d) confirm a strong thermal stability for PMI-[**F-OS**] and PMI-[**C-OS**]. Both acceptors show thermal decomposition above 400 °C, making them well suitable for OSC application. No glass transition temperatures or melting temperatures could be detected by DSC.

The permittivity of the new acceptors was determined from impedance spectroscopy. For this, we fabricated parallel-plate capacitors with ITO and Ag as bottom and top electrodes, and PEDOT:PSS as a smoothing layer, to obtain homogeneous acceptor layers. To account for thickness variations of the active material layers, the results were averaged from 20 to 30 measurements for each material. Compared to the reference compounds with alkyl chains, PMI-[**F-Alk**] and PMI-[**C-Alk**] (chemical structures see Scheme S1), the relative permittivity ε_r of the new acceptors with sulfone-ether side chains increased over the whole frequency range of 10^2 to 10^6 Hz (Figure 1c). Exemplary at 10^5 Hz, ε_r of PMI-[**F-OS**] and PMI-[**C-OS**] increased by 56% (from 1.86 to 2.90) and by 44% (from 1.91 to 2.76), respectively. In our recent work,[24] we have reported on the permittivity of related acceptors bearing diethylene glycol side chains. With respect to the same reference compounds, ε_r of these acceptors, PMI-[**F-OEG**] and PMI-[**C-OEG**], increased by 12% and 18%, respectively. Comparing the relative changes indicates a substantially greater influence of the new sulfone-ether chain on the material permittivity. In addition to the neat acceptors, we measured the permittivity of our final OSCs (vide infra). The obtained permittivity curves (Figure S30) show a more similar trend than the pristine acceptors. This can be explained by a larger contribution of the donor and interlayer materials. The stronger rise of the permittivity in the low frequency region (Hz−kHz) likely stems from the charged interlayers (PEDOT:PSS and PEIE:PFN-Br), where ionic contributions are dominant. However, to reduce exciton recombination, the permittivity is most crucial at the charge generation site (active layer, donor−acceptor interface). Therefore, the permittivity increase of the neat acceptors is likely a better indicator for the improvement in the active layer. These results underline sulfone groups as effective functionality for permittivity modification.

To gather further information that simplifies the later OSC optimization, we conducted solubility measurements, characterized the crystallinity and molecular packing, determined the frontier molecular orbital (FMO) energies, and measured the surface free energies (SFE) of the new acceptors. The solubility measurements (Table 2 and Table S1) revealed a significant difference between PMI-[**F-OS**] and PMI-[**C-OS**]. The fluorene-based acceptor with two side chains PMI-[**F-OS**] has better solubility in all tested solvents than PMI-[**C-OS**]. The highest solubility of PMI-[**F-OS**] is observed in chloroform (41.4 mg ml^{-1}) followed by THF (11.7 mg ml^{-1}) and DMF (7.0 mg ml^{-1}). The polar sulfone side chains exhibit a strong impact on the solubility in polar solvents. Interestingly, both acceptors show no solubility in *o*-xylene. From considering the results of the FMO and SFE measurements (vide infra), PTQ10 was selected as the most suitable polymer donor for PMI-[**F-OS**]. Because PTQ10 is in turn soluble in *o*-xylene (14.4 mg ml^{-1}, Table 2), a layer-by-layer processing of donor and acceptor becomes possible.

Table 2. Solubilities (in mg mL^{-1}) of the Acceptors PMI-[F-OS], PMI-[C-OS] and the Donor Polymer PTQ10 in Various Solvents

solvent	PTL[a]	PMI-[**F-OS**]	PMI-[**C-OS**]	PTQ10
chloroform	red	41.4	7.4	16.9
chlorobenzene	red	4.2	0.1	22.1
N,N-dimethylformamide	red	7.0	0.4	0.07
1,4-dioxane	red	2.2	0.8	0.07
o-xylene	orange	0.3	-	14.4
dimethyl sulfoxide	orange	1.6	0.3	0.07
tetrahydrofuran	orange	11.7	1.9	2.6
ethyl acetate	green	0.1	0.03	0.07
2-propanol	green	-	-	0.07

[a]Colors according to the Pfizer "traffic light" (PTL) solvent preference system (red...undesirable, orange...usable, green...preferable).[42]

The GIWAXS images (Figure 2) reveal a significantly higher crystallinity of PMI-[**C-OS**] compared to PMI-[**F-OS**]; however, there is an isotropic orientation with respect to the substrate observed in both samples. For PMI-[**C-OS**], a $\pi-\pi$ stacking distance of 0.35 nm is obtained (distinct peak at 18.0 nm^{-1}), while for PMI-[**F-OS**] the corresponding peak is markedly broadened, less pronounced, and slightly shifted to lower *q*-values (17.7 nm^{-1}), indicating less order and a slightly higher $\pi-\pi$ stacking distance. Moreover, regarding the lamellar stacking, PMI-[**C-OS**] shows a two-dimensional order indicated by the distinct peaks at 4.25, 3.43, and 2.42 nm^{-1} corresponding to lamellar *d* spacings of 1.5, 1.8, and 2.6 nm. In PMI-[**F-OS**], this structure is significantly less defined and spacings of 1.5 and 2.3 nm are found. The broad semicircle-shaped feature with a maximum at approx. 8.5 nm^{-1} observed in both samples corresponds most presumably to the 200 lamellar diffraction peaks.

The FMO energies (HOMO − highest occupied molecular orbital, LUMO − lowest unoccupied molecular orbital) were

https://doi.org/10.1021/acsaem.2c03433
ACS Appl. Energy Mater. 2023, 6, 1544−1554

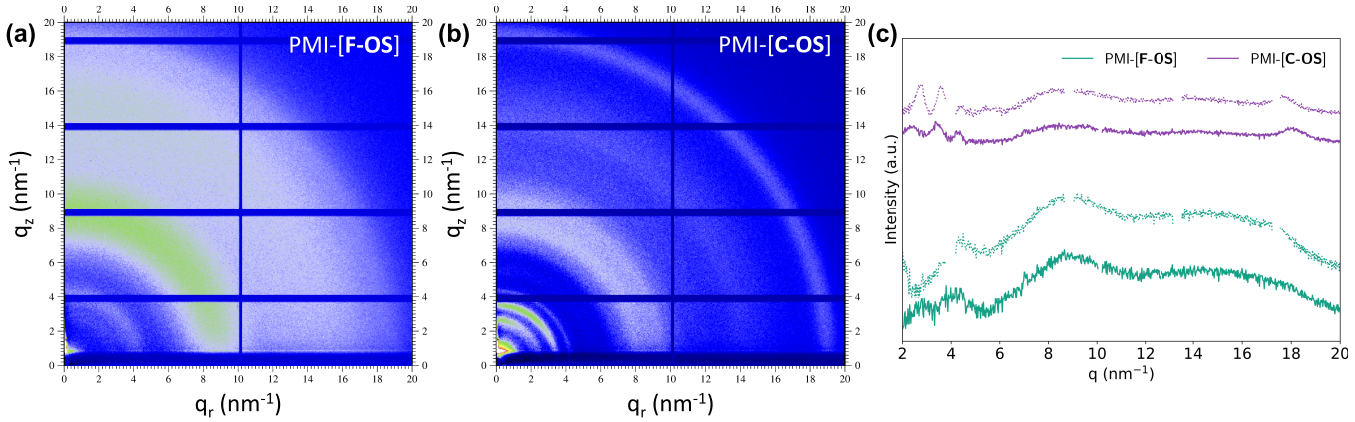

Figure 2. 2D GIWAXS images of (a) PMI-[**F-OS**], (b) PMI-[**C-OS**] and (c) the respective line cuts in in-plane (solid lines) and out-of-plane (dotted lines) direction. Measurements were acquired from drop-cast films on Si substrates.

obtained from cyclic voltammetry (CV) measurements of drop-cast films (Figure S18). PMI-[**F-OS**] and PMI-[**C-OS**] show HOMO/LUMO energies of −6.10/−4.03 eV and −6.07/−4.10 eV, respectively (Figure 3). From the three

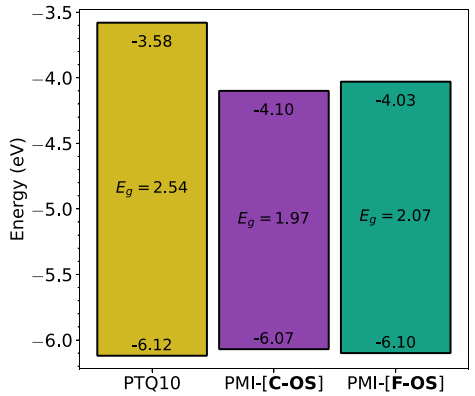

Figure 3. FMO energies (HOMO, LUMO) and the electrochemical bandgap (E_g) energies extracted from CV measurements (CV measurement: 3-electrode setup, drop-cast films on Pt disc working electrode, Pt wire counter electrode, non-aqueous $Ag/AgNO_3$ reference electrode, 0.1 M $TBAPF_6$ in acetonitrile as electrolyte, scan speed 50 mV s^{-1}). For CV measurements, see Figure S18.

commercially available donor polymers PM6, PBDB-T, and PTQ10, the latter two have suitable LUMO levels (Figure S18). The HOMO energy of PTQ10 seems critically low for efficient hole transfer. However, the small energy offset to the acceptors might be well within the measurement accuracy of the CV measurement for orbital energies, which is considered to be well above 0.1 eV for polymer films.[35] This was supported by initial tests of various polymers in OSCs, from which PTQ10 achieved the highest efficiencies. On the positive side, the small HOMO energy offset could promise a potentially high V_{OC} in OSCs. Further considering the energy levels of PTQ10, it is interesting to note that the electrochemical bandgap (2.54 eV, obtained from CV, Figure 3) is substantially larger than the optical bandgap (1.95 eV, obtained from thin film UV−Vis measurement, Figure 1b). This can be partly explained by the exciton binding energy in PTQ10 (0.31 eV[36]), which is defined as the difference of electrochemical and optical bandgap of a material.[37] Another reason can be factors such as solvent swelling and kinetic overpotential during the CV measurement.[38]

Lastly, it is crucial to know if the polymer and acceptor are energetically suitable in terms of their SFE. Since the SFE characteristics dominate the miscibility behavior of two materials, careful matching of donor and acceptor is vital to achieve an ideal active layer morphology. To determine the SFE values, we conducted contact angle measurements of pristine thin films with drops of water and ethylene glycol (EG). From that, we calculated the SFE values using the methods by Owens, Wendt, Rabel, and Kaelble (OWRK)[39] and Wu[40] (Table S2), and subsequently the Flory−Huggins interaction parameters χ for various donor−acceptor combinations (Table S3). χ should neither be too low (perfect miscibility, no pure domains) nor too high (zero miscibility, full demixing). The interaction parameters indicate that PMI-[**F-OS**] has a certain miscibility with the measured polymers (PTQ10, PM6, and PBDB-T), with χ values of 0.70, 0.80, and 0.63, respectively. PMI-[**C-OS**] on the other hand is expected to have a lower miscibility, with χ values of 2.04, 2.20, and 1.93, respectively.

Based on the CV and SFE measurements and due to its good solubility in the non-halogenated solvent *o*-xylene, we chose PTQ10 as the most suitable donor polymer. It is furthermore an attractive choice due to its simple and low-cost synthesis.[41] With this material combination, we can process donor and acceptor layer-by-layer with orthogonal, non-halogenated solvents (THF for PMI[**F-OS**] and *o*-xylene for PTQ10).

Design of Experiment. The orthogonal solvent systems for donor and acceptor simplify the use of a bilayer setup. This brings the advantage, compared to the BHJ system, that a separate optimization of donor and acceptor processing can be done. That way, the limitations imposed by the differences in solubility and SFE, caused by the polar sulfone chains, are reduced. Specifically, we used the conventional bilayer OSC setup ITO/PEDOT:PSS/PTQ10/acceptor/PEIE:PFN-Br/Ag. When testing PMI-[**C-OS**], strong aggregation was observed in all acceptor films due to the low solubility and high crystallinity of PMI-[**C-OS**]. This led to low solar cell performance (highest achieved PCE 1.2%, see Figure S28). Thus, after initial testing, we neglected PMI-[**C-OS**] and focused on the more promising PMI-[**F-OS**]. For this acceptor, AFM images (Figure S29) of a typical solar cell were recorded. These revealed a smooth and homogeneous film after the coating of

https://doi.org/10.1021/acsaem.2c03433
ACS Appl. Energy Mater. 2023, 6, 1544−1554

the PTQ10 layer from *o*-xylene. After the subsequent coating of the PMI-[**F-OS**] film on the PTQ10 layer, the surface morphology becomes slightly coarser; however, the appearance of the surface is homogeneous and a low surface roughness (root-mean-square S_q) of 1.4 nm is found, which is just slightly higher than for the PTQ10 film (S_q 1.1 nm).

A common challenge during OSC optimization is that it is a multivariate system involving numerous factors that can be varied. Even after the selection of active layer components (and their solvents) is done, many parameters remain to be optimized, such as the layer thicknesses of donor and acceptor, solvent additives, and thermal annealing conditions (temperature, duration, order of annealing). To find the optimum processing parameters, the classical approach is to screen over every factor separately, while keeping all others constant. This is repeated until a supposed optimum for all parameters is found. This so-called one-variable-at-a-time (OVAT) approach is highly time and resource consuming. Neither does it guarantee that the global optimum is indeed found since it completely disregards the mutual influence that factors have on each other. Therefore, we use a DoE approach, which was designed to solve multivariate problems in an efficient way. The DoE method covers a larger screening space more quickly and thoroughly and is more likely to yield the true optimum. DoE is already well described in the literature,[28−30] and specialized software is commercially available to help reduce the complexity of this approach significantly. In this work, we chose the software MODDE.[43]

As a first step, we defined the system by choosing a set of factors (processing parameters to be optimized, Table 3) and

Table 3. List of Factors in the DoE Analysis with Their Respective Levels

factor	unit	no. of levels	levels
RPM-D	rpm	3	1000, 3000, 5000
RPM-A	rpm	3	1000, 3000, 5000
TA-D	°C	3	25[a], 87.5, 150
TA-DA	°C	3	25[a], 87.5, 150

[a]TA of 25 °C corresponds to no annealing.

the intervals of interest (levels): the spin coating speeds (RPM-*D*, RPM-A) and the annealing temperatures after coating of the donor layer (TA-D) and acceptor layer (TA-DA), respectively. To limit the number of factors, the TA duration was set constant to 10 min, after which the further change of the thin film morphology should be small. To reduce the model size further, we set the concentrations of the donor and acceptor solutions to 8 mg ml^{-1}, respectively, to be well within the solubility ranges. To screen over a wide layer thickness range, the spin coating speed was varied over a large interval (1000 to 5000 rpm, respectively).

In the second step, we defined measurable responses. For that, we chose the typical OSC performance parameters PCE, fill factor (FF), short-circuit current density (J_{SC}), and open-circuit voltage (V_{OC}). After selecting factors, levels, and responses, we chose a D-optimal design for this optimization (design comparison and summary of model parameters, see Figure S19 and Table S4). As result, we obtained an experimental matrix with 24 experiments (Table S5), for which we built one substrate containing six separate OSCs for each experiment. The obtained model achieved a high quality of fit, summarized in Figure S20 and Figure S21. The results are shown as a 4D contour plot of the PCE behavior as function of the chosen factors (see Figure 4, contour plots for the FF, J_{SC}, and V_{OC}, see Figures S22−S24). The contour plot shows that the PCE is influenced by all four factors. A global maximum within the investigated parameter space is indicated in red. Further, the contour plots and especially the model coefficients (Table S6) show that indeed non-linear (quadratic and interaction) dependencies between the factors are present, which could not have been captured using the conventional OVAT method.

As an optimal setpoint, the model predicted the following processing parameters to obtain a maximum PCE of 4.37% (see Figure S25): RPM-D 3878 rpm, RPM-A 5000 rpm, TA-D 39 °C (almost RT, equivalent to no TA), TA-DA 25 °C (RT, equivalent to no TA). To validate the model, a control OSC series (48 solar cells on 8 substrates) was built with following parameters: RPM-D 3900 rpm (resulting layer thickness 16 ± 5 nm), RPM-A 5000 rpm (resulting layer thickness 48 ± 9 nm), no TA of the donor layer, no TA of the donor-acceptor layer. The control series achieved a top PCE of 4.55% (average 4.0 ± 0.7% from the best 5 cells), which is in excellent agreement with the model prediction. Interestingly, the most efficient OSCs are obtained without any TA treatment. Upon annealing, all solar cells experience a drop in J_{SC} and FF, which manifests also in the 4D contour plots of the FF and J_{SC} (Figures S22 and S23). We assume that this is because the interface of donor and acceptor changes for the worse. The formation of a mixed D/D:A/A-like structure was proven to be desirable to increase the interface area of donor and acceptor and reduce recombination losses.[44,45] Using THF as the acceptor solvent, in which PTQ10 also shows slight solubility (2.6 mg ml^{-1}), should support formation of this intermixed domain, whereas annealing treatment seems to have a negative effect. GIWAXS measurements of the bilayer were conducted; however, the low signal intensity did not allow to make clear statements about the morphology change upon annealing.

The DoE analysis proved to be efficient and reliable for OSC optimization. It yielded the optimal processing conditions for four factors within little time and with only few resources used. The predicted optimum was congruent with the experimental test. As a next step, we conducted thorough characterization with the optimized OSCs.

Solar Cell Characterization. To gain insights into the photovoltaic properties of the optimized OSCs with the device architecture shown in Figure 5a, we measured their current density−voltage (*JV*) and external quantum efficiency (EQE) characteristics and light intensity dependencies and performed stability tests. The *JV* measurements revealed a significant positive light soaking effect for all OSCs, where 10−30 min of light soaking led to an increase in both J_{SC} and FF, which increased the PCE by up to one percentage point. This can most likely be explained by a combined effect of first filling up recombination sites, which reduces the bimolecular recombination rate and thus improves the J_{SC}, and second a very mild annealing effect that can potentially improve the interplay of all layers in the final OSCs. Both effects can be especially strong because of the small orbital energy offset of PTQ10 and PMI-[**F-OS**]. For that reason, all results and further OSC characterization are shown for light-soaked solar cells.

With the optimized device setup (obtained from the DoE analysis), we achieved a PCE of 5.2 ± 0.2% (top 5.51%), combined with a high V_{OC} of 1.296 ± 0.006 V (top 1.298 V) (summary, see Table 4; *JV* curves, Figure 5b). The EQE

https://doi.org/10.1021/acsaem.2c03433
ACS Appl. Energy Mater. 2023, 6, 1544−1554

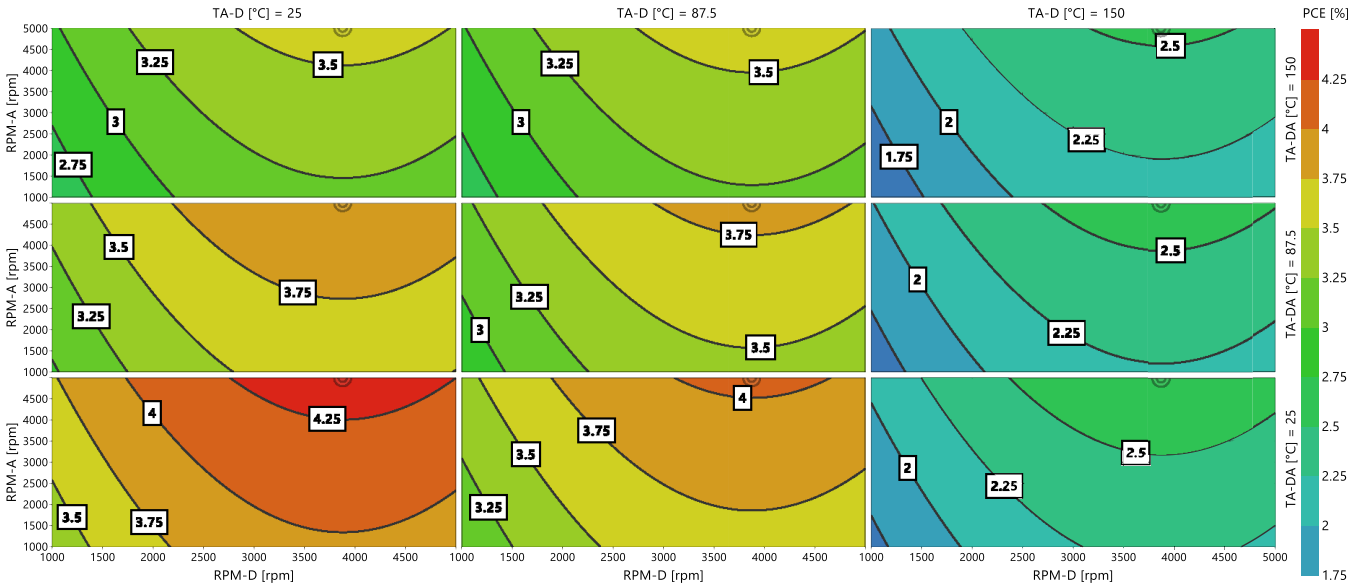

Figure 4. DoE 4D contour plot of the resulted fitting model for the **PCE** of the OSC system ITO/PEDOT:PSS/PTQ10/PMI-[**F-OS**]/PEIE:PFN-Br/Ag. The factor levels (RPM-D, RPM-A, TA-D and TA-DA) are on the outer sides of the contour plots. The PCE is shown as colored area (legend on the right side, red indicates the highest value). The optimal setpoint was calculated to be at RPM-D 3878 rpm, RPM-A 5000 rpm, TA-D 39 °C, and TA-DA 25 °C.

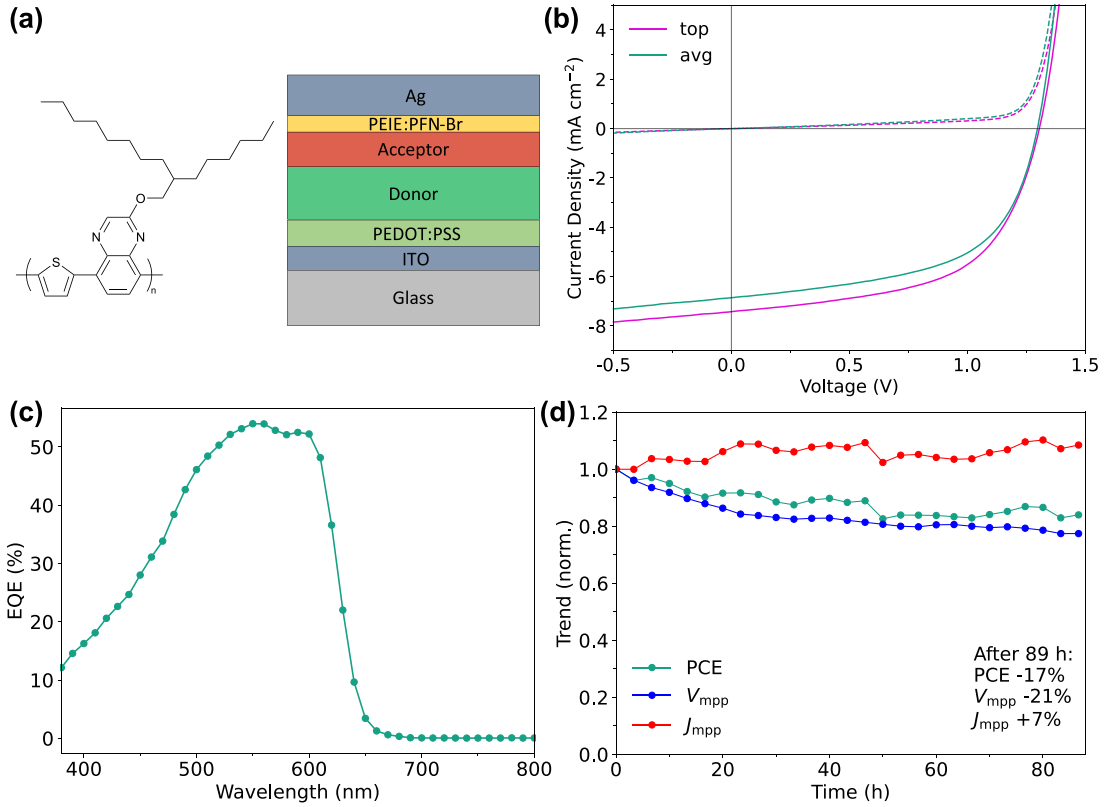

Figure 5. Solar cell characterization of the best OSC setup ITO/PEDOT:PSS/PTQ10/PMI-[**F-OS**]/PEIE:PFN-Br/Ag. (a) Structure of PTQ10 and schematic cross section of the used bilayer setup. (b) *JV* characteristic of the best cell (top) and a cell similar to the average values (avg), both in illuminated (solid) and dark (dashed) conditions. (c) EQE spectrum of an average OSC. (d) Stability test of a solar cell operated at the maximum power point (mpp) under constant illumination of 100 mW cm^{-2} in inert conditions.

measurement (Figure 5c) shows a maximum value of 55% between 520 and 620 nm and a shape that fits well with the absorption behavior of PTQ10:PMI-[**F-OS**] thin films (Figure 1b). The PCE of these solar cells surpasses the performance of OSCs based on the reference compound PMI-[**F-Alk**] (PCE 4.34 ± 0.37% with 1.09 ± 0.04 V).[31] For a direct comparison, we also built OSCs in the identical BHJ setup used in the reference system (ITO/ZnO/PBDB-T:PMI-[**F-OS**]/MoO_3/Ag). The results are summarized in Table S8 and Figure S28. The highest PCE was 3.13%, with a generally low FF and J_{SC}.

https://doi.org/10.1021/acsaem.2c03433
ACS Appl. Energy Mater. 2023, 6, 1544−1554

Table 4. Summary of OSC Data[a]

type	t_D (nm)	t_A (nm)	V_{OC}(V)	J_{SC} (mA cm^{-2})	FF (%)	PCE (%)	R_s[b] (Ω cm^2)	R_{sh}[b] (Ω cm^2)
top			1.298	7.42	57.5	5.51	0.702	985.3
avg[c]	16 ± 5	48 ± 9	1.296 ± 0.006	7.1 ± 0.2	57 ± 1	5.2 ± 0.2	0.457	923.7

[a]Of devices with the ITO/PEDOT:PSS/PTQ10/PMI-[**F-OS**]/PEIE:PFN-Br/Ag bilayer setup. All values were recorded after light soaking. [b]Extracted from fitting the single-diode equivalent circuit model[46] to the *JV* curves of the top solar cell and a solar cell that has characteristic values similar to the average parameters (full fitting data, see Table S7 and Figure S26b). [c]Average values (arithmetic mean and standard deviation) are calculated from the 10 best cells.

Vice versa, we also built bilayer OSCs with the reference acceptor (ITO/PEDOT:PSS/PTQ10/PMI-[**F-Alk**]/PEIE:PFN-Br/Ag). This combination showed a significantly inferior efficiency, with a top PCE of 0.96% and V_{OC} of 1.25 V (see Table S9 and Figure S28c), which could be explained by the lower permittivity of PMI-[**F-Alk**] (permittivity measurements of whole OSCs, see Figure S30) and a more complicated preparation (PMI-[**F-Alk**] only processable from chlorobenzene).

Our results show that with all changes, we achieved to employ a high-ε acceptor in OSCs with improved efficiencies. To combine the advantages of high-ε materials with the generally higher currents obtained when using the bulk heterojunction setup, a possible outlook is to modify both, donor and acceptor, with similar polar side chains. This could lead to a better interaction and similar solubility of both materials, enabling higher efficiencies.

In addition to *JV* measurements, we conducted stability tests by maximum-power-point tracking in illuminated conditions inside a nitrogen glove box (Figure 5d). After 89 h, the PCE still was 83% of the initial value, whereby the main loss was observed in the first 25 h followed by only a minor decrease after this point. To get insights into the recombination properties within the OSCs, we measured the light intensity dependence of V_{OC} and J_{SC} (Figure S26d–f). The J_{SC} trend has a slope of 0.99, which indicates that monomolecular recombination pathways dominate under short-circuit conditions.[47] Further, the V_{OC} trend from 10 to 100 mW cm^{-2} shows an ideality factor of 1.78, which indicates that Shockley–Reed–Hall recombination dominates under open-circuit conditions.[48] This is in good agreement with the extracted ideality factor of approx. 2 from the dark *JV* curve fitting (Table S7). We then investigated the charge-generation efficiencies, by plotting a J_{ph}–V_{eff} curve for an average bilayer OSC (Figure S27). From this, we calculated the exciton dissociation efficiency (η_{diss}) as well as the charge collection efficiency (η_{cc}) (calculation procedure see the Supporting Information). A η_{diss} of 95% and η_{cc} of 74% suggest a highly efficient dissociation of formed excitons into free charge carriers under short-circuit conditions, and a good charge collection at maximum power point conditions.

Lastly, the high V_{OC} motivated us to compare the energy losses of the fabricated devices (Table S10). Of all compared setups, the bilayer OSCs containing PMI-[**F-OS**] showed the lowest overall energy loss of 0.66 eV, compared to 0.70 and 0.73 eV of the reference setups.

CONCLUSIONS

In this work, we introduced polar sulfone side chains to known non-fullerene acceptors with the aim of increasing their dielectric permittivity. The new acceptors, named PMI-[**F-OS**] and PMI-[**C-OS**], exhibited a permittivity increase by 56% (ε_r from 1.86 to 2.90) and by 44% (ε_r from 1.91 to 2.76) at 10^5 Hz. Simultaneously, resulting from the sulfone modification, PMI-[**F-OS**] shows a high solubility (11.7 mg ml^{-1}) in THF. The solar cells were built in a conventional bilayer setup (ITO/PEDOT:PSS/PTQ10/PMI-[**F-OS**]/PEIE:PFN-Br/Ag), using only non-halogenated solvents (*o*-xylene for the donor polymer PTQ10 and THF for the acceptor). The optimization of the processing parameters of the solar cells was successfully conducted with the resource- and time-saving DoE method, an approach still underrepresented in solar cell research. That way, only a small number of experiments were needed to obtain the desired PCE maximum. The optimized OSCs achieved a PCE of 5.2 ± 0.2% (best 5.51%) with a high V_{OC} of 1.296 ± 0.006 V (best 1.298 V), surpassing the performance of solar cells containing the alkylated analog[31] of PMI-[**F-OS**], with the additional benefit of the processing from non-halogenated solvents.

Our findings clearly show that a bilayer OSC setup can prevent efficiency losses typically stemming from unfavorable donor–acceptor phase separation in bulk heterojunction OSCs due to significantly changed surface free energy and solubility of high-ε materials. This work can provide a valuable tool for further research on high-ε materials and to unfold the full potential of permittivity-engineering toward improving the overall performance of OSCs. We also envision that this approach might be applied in the future to more efficient materials, such as the popular Y series acceptors.

EXPERIMENTAL SECTION

Synthesis. All reagents and solvents were purchased from commercially available sources (Sigma Aldrich, Lumtec, abcr, VWR, Roth) and used as received, unless otherwise stated. 2,7-Dibromofluorene and 2,7-dibromo-9*H*-carbazole were dried in vacuum over $CaCl_2$ before use. PPh_3 was recrystallized from EtOH before use. Anhydrous CH_2Cl_2 was prepared by distillation over P_4O_{10}. Anhydrous THF was prepared by running the solvent through an automated aluminum oxide column. Dry MeCN (99.8% purity grade) was purchased from Merck. The polymers for solar cell processing, PTQ10 and PFN-Br, were purchased from 1-Material. PEDOT:PSS was purchased from Heraeus (CLEVIOS P VP AI 4083). Here listed are the novel synthetic steps toward PMI-[**F-OS**]. All remaining synthetic procedures are attached in the Supporting Information.

*1-Bromo-3-(2-(methylsulfonyl)ethoxy)propane ($C_6H_{13}BrO_3S$) (**1**).* The procedure was adapted from the literature.[49] Methyl vinyl sulfone (1.44 mL, 1.73 g, 16.3 mmol, 1.0 equiv), 3-bromopropan-1-ol (2.20 mL, 3.40 g, 24.5 mmol, 1.5 equiv), and PPh_3 (0.428 g, 1.63 mmol, 0.1 equiv) were dissolved in 15 mL of CH_2Cl_2 anh. The flask was flushed with nitrogen and the reaction was stirred at RT overnight. A yellow solution with a colorless precipitate had formed. Full conversion was controlled by TLC and APCI-MS. For workup, the CH_2Cl_2 was evaporated in a nitrogen stream, and then the liquid and solid residue were dispersed in 5 mL of ethyl acetate and filtered. The filter cake was washed several times with ethyl acetate. The filtrate was concentrated *in vacuo*, and the clear yellow oily residue was purified by column chromatography (eluent gradient CH:EA 5:1 to pure EA). This gave the product **1** (2.63 g, 66%) as a colorless oil.

https://doi.org/10.1021/acsaem.2c03433
ACS Appl. Energy Mater. 2023, 6, 1544–1554

R_f 0.45 (CH:EA 1:5). ^{1}H NMR (300 MHz, $CDCl_3$, TMS) δ (ppm): 3.90 (t, J = 5.3 Hz, 2 H), 3.64 (t, J = 5.9 Hz, 2 H), 3.48 (t, J = 6.4 Hz, 2 H), 3.23 (t, J = 5.3 Hz, 2 H), 2.99 (s, 3 H), 2.12 (tt, J = 5.9, 6.4 Hz, 2 H). ^{13}C NMR (75 MHz, $CDCl_3$, TMS) δ (ppm): 68.8, 64.7, 55.3, 43.0, 32.3, 30.0. MS (APCI) calcd. For $C_6H_{14}BrO_3S^+$ $[M + H]^+$ m/z: 244.98, found 245.0.

*2,7-Dibromo-9,9-bis(3-(2-(methylsulfonyl)ethoxy)propyl)-9H-fluorene ($C_{25}H_{32}Br_2O_6S_2$) (**4**).* The procedure was adapted from the literature.[50] A round-bottom flask was charged with 2,7-dibromofluorene (994 mg, 3.06 mmol, 1.0 equiv) and crushed KOH (368 mg, 9.2 mmol, 3.0 equiv) and then flushed with nitrogen for 10 min. MeCN (50 mL) was added, and after 10 min, compound **1** (2.25 g, 9.2 mmol, 3.0 equiv) was added dropwise, upon which the reaction mixture immediately turned dark blue. The mixture was stirred at RT overnight. After TLC control, the dark blue reaction mixture was quenched by adding water until full dissolution of all KOH and then extracted with CH_2Cl_2 (3×). The combined organic phase (clear orange) was washed with water and brine, dried over Na_2SO_4, and concentrated *in vacuo*. The crude product (orange oil) was purified by column chromatography (gradient CH:THF 2:1 to pure THF). This gave the product **4** (752 mg, 38%) as a colorless solid.

R_f 0.4 (CH:EA 1:1). ^{1}H NMR (300 MHz, $CDCl_3$, TMS) δ (ppm): 7.62−7.37 (m, 6 H), 3.68 (t, J = 5.2 Hz, 4 H), 3.26−3.08 (m, 8 H), 2.93 (s, 6 H), 2.13−1.96 (m, 4 H), 0.94−0.73 (m, 4 H). MS (APCI) m/z for $C_{25}H_{33}Br_2O_6S_2^+$ $[M + H]^+$: calcd. 651.00, found 651.0.

*8,8′-(9,9-Bis(3-(2-(methylsulfonyl)ethoxy)propyl)-9H-fluorene-2,7-diyl)bis(2-(2,6-diisopropylphenyl)-1H-benzo[10,5]anthra[2,1,9-def]isoquinoline-1,3(2H)-dione) ($C_{93}H_{84}N_2O_{10}S_2$) (PMI-[**F-OS**]).* A 3-neck round bottom flask with a reflux condenser, dropping funnel, and nitrogen inlet was charged with compound **4** (0.654 g, 1.00 mmol, 1.0 equiv), aqueous 1 M K_2CO_3 solution (15 mL), Aliquat 336 (2−3 drops), and THF (100 mL). **6c** (1.463 g, 2.41 mmol, 2.4 equiv) was dissolved in THF (60 mL) and transferred to the dropping funnel. Both solutions were degassed for 15 min by bubbling nitrogen gas through the solutions. Afterward, the catalyst $[Pd(PPh_3)_4]$ (58 mg, 0.050 mmol, 0.050 equiv) was added, the flask heated to reflux and **6c** added in four portions (next portion added only when TLC control indicated full consumption of **6c**, to prevent side product formation). After TLC control indicated full conversion, the THF was evaporated *in vacuo*. The residue was dissolved in CH_2Cl_2, washed with water (3×) and brine, dried over Na_2SO_4, and concentrated *in vacuo*. The crude product was purified by column chromatography (gradient CH_2Cl_2:acetone 3% to 6%) followed by recrystallization. For that, we dissolved the crude in 100 mL of hot THF and added toluene until mild precipitation was observed (approx. 100 mL). After cooling to RT, it was put in a fridge (8 °C) overnight. This gave PMI-[**F-OS**] (480 mg, 33%) as a red solid.

R_f 0.85 (CH_2Cl_2:acetone 10:1). UV−Vis $\lambda_{max}(CHCl_3)$/nm 527 (ε/dm^3 mol^{-1} cm^{-1} 8.53 × 10^4), 505sh (7.67 × 10^4). ^{1}H NMR (500 MHz, $CDCl_3$, TMS) δ (ppm): 8.67 (d, J = 7.9 Hz, 4 H), 8.54 (d, J = 8.0 Hz, 2 H), 8.49 (d, J = 7.6 Hz, 2 H), 8.48−8.43 (m, 4 H), 8.05 (d, J = 8.4 Hz, 2 H), 8.00 (d, J = 7.7 Hz, 2 H), 7.70 (d, J = 7.7 Hz, 2 H), 7.67−7.61 (m, 4 H), 7.59 (s, 2 H), 7.49 (t, J = 7.8 Hz, 2 H), 7.36 (J = 7.8 Hz, 4 H), 3.75 (t, J = 5.3 Hz, 4 H), 3.33 (t, J = 6.3 Hz, 4 H), 3.12 (t, J = 5.3 Hz, 4 H), 2.82 (s, 6 H), 2.79 (sept, J = 6.8 Hz, 4 H), 2.23 (m, 4 H), 1.25−1.09 (m, 28 H). ^{13}C NMR (125 MHz, $CDCl_3$, TMS) δ (ppm): 164.0, 150.3, 145.8, 143.3, 140.6, 139.4, 137.5, 137.3, 132.7, 132.1, 131.1, 130.5, 129.8, 129.6, 129.5, 129.0, 128.8, 128.5, 128.4, 127.1, 126.9, 124.5, 124.1, 123.5, 121.1, 121.0, 120.5, 120.4, 120.2, 77.3, 71.6, 64.3, 55.2, 54.8, 43.0, 36.8, 29.2, 24.4, 24.1. HR-MS (MALDI-TOF) m/z for $C_{93}H_{85}N_2O_{10}S_2^+$ $[M + H]^+$: calcd. 1453.5646, found 1453.3782.

Solar Cell Fabrication. Solar cell fabrication was done in a conventional bilayer setup. For preparation, pre-patterned glass/ITO substrates (15 × 15 × 1.1 mm^3, 15 Ω sq.$^{-1}$) were cleaned by wiping them with acetone using Kimwipes (Kimberly-Clark), then by sonication in a 2-propanol bath (40 °C, 30 min) followed by blow-drying in a nitrogen stream, and finally oxygen plasma etching (99 W, 3 min, FEMTO, Diener Electronics). For the conventional bilayer setup (ITO/PEDOT:PSS/donor/acceptor/PEIE:PFN-Br/Ag), a suspension of PEDOT:PSS in water was filtered through a 0.45 μm PVDF syringe filter and then spin-coated (50 μL with 3000 rpm and 2000 rpm s^{-1} for 40 s) onto freshly plasma-etched glass/ITO substrates followed by thermal annealing at 150 °C for 15 min in ambient conditions. For the active layer, separate precursor solutions (8 mg ml^{-1}) of PTQ10 in *o*-xylene and the respective acceptor in THF (and PMI-[**F-Alk**] in chlorobenzene) were prepared in the nitrogen glove box and stirred overnight at RT (acceptor solutions) or while heating at 60 °C (donor solutions). The layers were applied with varying spin coating parameters (1000−5000 rpm) and annealing strategies. The PTQ10 layers were spin-coated from hot solutions (60 °C). For the PEIE:PFN-Br layer, precursor solutions of both materials were made in a nitrogen glove box. The starting material for PEIE, a 37 wt % solution in water was diluted with MeOH to give a 5 mg mL^{-1} solution. Pristine PFN-Br was diluted with MeOH to give a 0.5 mg mL^{-1} solution. Briefly before deposition, the solutions were mixed in a ratio 1:10 v:v to obtain a 1:1 w:w ratio. The final solution was spin-coated (50 μL with 2000 rpm and 1500 rpm s^{-1} for 40 s) onto the active layer in inert conditions. Lastly, a Ag electrode (100 nm, 0.1−2.0 Å s^{-1}) layer was applied by thermal evaporation at high vacuum (<1 × 10^{-5} mbar, thickness monitor: Inficon SQM-160 rate/thickness monitor) through a shadow mask (3 × 3 mm^2).

Inverted solar cells were built in the following architecture: ITO/ZnO/active layer/MoO_3/Ag. For the ZnO precursor solution, 500 mg of zinc acetate dihydrate was dissolved in 5 mL of 2-methoxyethanol and 150 μL of ethanolamine as the stabilizer. The solution was stirred at least overnight and then filtered through a 0.45 μm PTFE syringe filter before use. The solution was spin coated (4000 rpm, 30 s) and annealed (150 °C, 15 min) in ambient conditions. For the active layers, precursor solutions were prepared (differing D/A ratios and total concentrations) stirred at 60 °C overnight. The layers were applied with varying spin coating parameters (1000 to 4000 rpm for 60 s, then drying at 5000 rpm for 5 s). Finally, the MoO_x (10 nm) and Ag (100 nm) layers were applied by thermal evaporation at high vacuum (<1 × 10^{-5} mbar) through a shadow mask (3 × 3 mm^2).

■ ASSOCIATED CONTENT

Supporting Information

The Supporting Information is available free of charge at https://pubs.acs.org/doi/10.1021/acsaem.2c03433.

Experimental methods, additional synthetic procedures, NMR and MS spectra, UV−Vis spectra, thermoanalysis, solubility data, contact angle measurements and surface free energy data, DoE specification and additional figures, *JV* curve fitting values, additional solar cell characterization, AFM images (PDF)

■ AUTHOR INFORMATION

Corresponding Authors

Thomas Rath − *Institute for Chemistry and Technology of Materials (ICTM), NAWI Graz, Graz University of Technology, 8010 Graz, Austria; Joanneum Research, MATERIALS-Institute for Surface Technologies and Photonics, 8160 Weiz, Austria;* orcid.org/0000-0002-4837-7726; Email: thomas.rath@tugraz.at

Gregor Trimmel − *Institute for Chemistry and Technology of Materials (ICTM), NAWI Graz, Graz University of Technology, 8010 Graz, Austria;* orcid.org/0000-0001-8922-4163; Email: gregor.trimmel@tugraz.at

Authors

Peter Fürk − *Institute for Chemistry and Technology of Materials (ICTM), NAWI Graz, Graz University of Technology, 8010 Graz, Austria;* orcid.org/0000-0001-5416-579X

Matiss Reinfelds − *Institute for Chemistry and Technology of Materials (ICTM), NAWI Graz, Graz University of Technology, 8010 Graz, Austria;* orcid.org/0000-0003-1745-014X
Ilie Hanzu − *Institute for Chemistry and Technology of Materials (ICTM), NAWI Graz, Graz University of Technology, 8010 Graz, Austria;* orcid.org/0000-0002-9260-9117
Theresa Hartl − *Institute for Chemistry and Technology of Materials (ICTM), NAWI Graz, Graz University of Technology, 8010 Graz, Austria*
Jana B. Schaubeder − *Institute of Bioproducts and Paper Technology, Graz University of Technology, 8010 Graz, Austria;* orcid.org/0000-0002-2384-333X
Elena Zuccala − *Institute for Chemistry and Technology of Materials (ICTM), NAWI Graz, Graz University of Technology, 8010 Graz, Austria;* orcid.org/0000-0002-3755-3958
Heinz Amenitsch − *Institute of Inorganic Chemistry, NAWI Graz, Graz University of Technology, 8010 Graz, Austria*

Complete contact information is available at: https://pubs.acs.org/10.1021/acsaem.2c03433

Notes

The authors declare no competing financial interest.

■ ACKNOWLEDGMENTS

Financial support by the Zukunftsfonds Steiermark (project: GreenOPVSolutions) is gratefully acknowledged. The authors also acknowledge the CERIC-ERIC Consortium for the access to experimental facilities (Austrian SAXS beamline at Elettra Sincrotrone Trieste) and financial support. The authors thank Petra Kaschnitz, Karin Bartl, Lukas Troi, and Matthias Schwar for their support.

■ REFERENCES

(1) Stephen, M.; Genevičius, K.; Juška, G.; Arlauskas, K.; Hiorns, R. C. Charge transport and its characterization using photo-CELIV in bulk heterojunction solar cells. *Polym. Int.* **2017**, *66*, 13−25.
(2) Cui, Y.; Yao, H.; Zhang, J.; Zhang, T.; Wang, Y.; Hong, L.; Xian, K.; Xu, B.; Zhang, S.; Peng, J.; Wei, Z.; Gao, F.; Hou, J. Over 16% efficiency organic photovoltaic cells enabled by a chlorinated acceptor with increased open-circuit voltages. *Nat. Commun.* **2019**, *10*, 2515.
(3) Søndergaard, R.; Hösel, M.; Angmo, D.; Larsen-Olsen, T. T.; Krebs, F. C. Roll-to-roll fabrication of polymer solar cells. *Mater. Today* **2012**, *15*, 36−49.
(4) Meng, D.; Sun, D.; Zhong, C.; Liu, T.; Fan, B.; Huo, L.; Li, Y.; Jiang, W.; Choi, H.; Kim, T.; Kim, J. Y.; Sun, Y.; Wang, Z.; Heeger, A. J. High-Performance Solution-Processed Non-Fullerene Organic Solar Cells Based on Selenophene-Containing Perylene Bisimide Acceptor. *J. Am. Chem. Soc.* **2016**, *138*, 375−380.
(5) Zhu, L.; Zhang, M.; Xu, J.; Li, C.; Yan, J.; Zhou, G.; Zhong, W.; Hao, T.; Song, J.; Xue, X.; Zhou, Z.; Zeng, R.; Zhu, H.; Chen, C.-C.; MacKenzie, R. C. I.; Zou, Y.; Nelson, J.; Zhang, Y.; Sun, Y.; Liu, F. Single-junction organic solar cells with over 19% efficiency enabled by a refined double-fibril network morphology. *Nat. Mater.* **2022**, *21*, 656−663.
(6) He, C.; Pan, Y.; Ouyang, Y.; Shen, Q.; Gao, Y.; Yan, K.; Fang, J.; Chen, Y.; Ma, C.-Q.; Min, J.; Zhang, C.; Zuo, L.; Chen, H. Manipulating the D:A interfacial energetics and intermolecular packing for 19.2% efficiency organic photovoltaics. *Energy Environ. Sci.* **2022**, *15*, 2537−2544.
(7) Koster, L. J. A.; Shaheen, S. E.; Hummelen, J. C. Pathways to a New Efficiency Regime for Organic Solar Cells. *Adv. Energy Mater.* **2012**, *2*, 1246−1253.
(8) Wannier, G. H. The Structure of Electronic Excitation Levels in Insulating Crystals. *Phys. Rev.* **1937**, *52*, 191−197.
(9) Kirchartz, T.; Pieters, B. E.; Kirkpatrick, J.; Rau, U.; Nelson, J. Recombination via tail states in polythiophene:fullerene solar cells. *Phys. Rev. B* **2011**, *83*, No. 115209.
(10) Langevin, P. Reunification and Mobility of the Ions in Gases. *Ann. Chim. Phys.* **1903**, *28*, 433−530.
(11) Liu, X.; Li, Y.; Ding, K.; Forrest, S. Energy Loss in Organic Photovoltaics: Nonfullerene Versus Fullerene Acceptors. *Phys. Rev. Appl.* **2019**, *11*, 24060.
(12) Brebels, J.; Manca, J. V.; Lutsen, L.; Vanderzande, D.; Maes, W. High dielectric constant conjugated materials for organic photovoltaics. *J. Mater. Chem. A* **2017**, *5*, 24037−24050.
(13) Leblebici, S. Y.; Chen, T. L.; Olalde-Velasco, P.; Yang, W.; Ma, B. Reducing exciton binding energy by increasing thin film permittivity: an effective approach to enhance exciton separation efficiency in organic solar cells. *ACS Appl. Mater. Interfaces* **2013**, *5*, 10105−10110.
(14) Leblebici, S.; Lee, J.; Weber-Bargioni, A.; Ma, B. Dielectric Screening To Reduce Charge Transfer State Binding Energy in Organic Bulk Heterojunction Photovoltaics. *J. Phys. Chem. C* **2017**, *121*, 3279−3285.
(15) Oh, J.; Jung, S.; Jeong, M.; Lee, B.; Lee, J.; Cho, Y.; Lee, S. M.; Chen, S.; Zhang, Z.-G.; Li, Y.; Yang, C. Ring-perfluorinated non-volatile additives with a high dielectric constant lead to highly efficient and stable organic solar cells. *J. Mater. Chem. C* **2019**, *7*, 4716−4724.
(16) Mishima, K.; Sakai, T.; Yokota, K.; Taniguchi, M.; Aso, Y.; Ie, Y.; Yamashita, K. The effect of a two-dimensional structure on the dielectric constant and photovoltaic characteristics. *J. Photochem. Photobiol. A* **2020**, *401*, No. 112756.
(17) Zhang, X.; Zhang, D.; Zhou, Q.; Wang, R.; Zhou, J.; Wang, J.; Zhou, H.; Zhang, Y. Fluorination with an enlarged dielectric constant prompts charge separation and reduces bimolecular recombination in non-fullerene organic solar cells with a high fill factor and efficiency > 13%. *Nano Energy* **2019**, *56*, 494−501.
(18) Sami, S.; Alessandri, R.; Broer, R.; Havenith, R. W. A. How Ethylene Glycol Chains Enhance the Dielectric Constant of Organic Semiconductors: Molecular Origin and Frequency Dependence. *ACS Appl. Mater. Interfaces* **2020**, *12*, 17783−17789.
(19) Brebels, J.; Douvogianni, E.; Devisscher, D.; Thiruvallur Eachambadi, R.; Manca, J.; Lutsen, L.; Vanderzande, D.; Hummelen, J. C.; Maes, W. An effective strategy to enhance the dielectric constant of organic semiconductors − CPDTTPD-based low bandgap polymers bearing oligo(ethylene glycol) side chains. *J. Mater. Chem. C* **2018**, *6*, 500−511.
(20) Wang, C.; Zhang, Z.; Pejić, S.; Li, R.; Fukuto, M.; Zhu, L.; Sauvé, G. High Dielectric Constant Semiconducting Poly(3-alkylthiophene)s from Side Chain Modification with Polar Sulfinyl and Sulfonyl Groups. *Macromolecules* **2018**, *51*, 9368−9381.
(21) Torabi, S.; Jahani, F.; van Severen, I.; Kanimozhi, C.; Patil, S.; Havenith, R. W. A.; Chiechi, R. C.; Lutsen, L.; Vanderzande, D. J. M.; Cleij, T. J.; Hummelen, J. C.; Koster, L. J. A. Strategy for Enhancing the Dielectric Constant of Organic Semiconductors Without Sacrificing Charge Carrier Mobility and Solubility. *Adv. Funct. Mater.* **2015**, *25*, 150−157.
(22) Liu, X.; Xie, B.; Duan, C.; Wang, Z.; Fan, B.; Zhang, K.; Lin, B.; Colberts, F. J. M.; Ma, W.; Janssen, R. A. J.; Huang, F.; Cao, Y. A high dielectric constant non-fullerene acceptor for efficient bulk-heterojunction organic solar cells. *J. Mater. Chem. A* **2018**, *6*, 395−403.
(23) Atkins, P. W.; de Paula, J.. *Physical Chemistry*; Oxford University Press: Oxford, 2006; pp. 627−629.
(24) Fürk, P.; Hofinger, J.; Reinfelds, M.; Rath, T.; Amenitsch, H.; Scharber, M. C.; Trimmel, G. Glycol bearing perylene monoimide based non-fullerene acceptors with increased dielectric permittivity. *Monatsh. Chem.* **2022**, DOI: 10.1007/s00706-022-02956-2.
(25) Zhang, S.; Zhang, Z.; Liu, J.; Wang, L. Fullerene Adducts Bearing Cyano Moiety for Both High Dielectric Constant and Good Active Layer Morphology of Organic Photovoltaics. *Adv. Funct. Mater.* **2016**, *26*, 6107−6113.

(26) Donaghey, J. E.; Armin, A.; Burn, P. L.; Meredith, P. Dielectric constant enhancement of non-fullerene acceptors via side-chain modification. *Chem. Commun.* **2015**, *51*, 14115−14118.
(27) Jang, B.; Lee, C.; Lee, Y. W.; Kim, D.; Uddin, M. A.; Kim, F. S.; Kim, B. J.; Woo, H. Y. A High Dielectric N-Type Small Molecular Acceptor Containing Oligoethyleneglycol Side-Chains for Organic Solar Cells. *Chin. J. Chem.* **2018**, *36*, 199−205.
(28) Cao, B.; Adutwum, L. A.; Oliynyk, A. O.; Luber, E. J.; Olsen, B. C.; Mar, A.; Buriak, J. M. How To Optimize Materials and Devices via Design of Experiments and Machine Learning: Demonstration Using Organic Photovoltaics. *ACS Nano* **2018**, *12*, 7434−7444.
(29) Leardi, R. Experimental design in chemistry: A tutorial. *Anal. Chim. Acta* **2009**, *652*, 161−172.
(30) Kirkey, A.; Luber, E. J.; Cao, B.; Olsen, B. C.; Buriak, J. M. Optimization of the Bulk Heterojunction of All-Small-Molecule Organic Photovoltaics Using Design of Experiment and Machine Learning Approaches. *ACS Appl. Mater. Interfaces* **2020**, *12*, 54596−54607.
(31) Weber, S.; Hofinger, J.; Rath, T.; Reinfelds, M.; Pfeifer, D.; Borisov, S. M.; Fürk, P.; Amenitsch, H.; Scharber, M. C.; Trimmel, G. Comparison of fluorene, silafluorene and carbazole as linkers in perylene monoimide based non-fullerene acceptors. *Mater. Adv.* **2020**, *1*, 2095−2106.
(32) Hofinger, J.; Weber, S.; Mayr, F.; Jodlbauer, A.; Reinfelds, M.; Rath, T.; Trimmel, G.; Scharber, M. C. Wide-bandgap organic solar cells with a novel perylene-based non-fullerene acceptor enabling open-circuit voltages beyond 1.4 V. *J. Mater. Chem. A* **2022**, *10*, 2888−2906.
(33) Hu, Y.; Chen, S.; Zhang, L.; Zhang, Y.; Yuan, Z.; Zhao, X.; Chen, Y. Facile Approach to Perylenemonoimide with Short Side Chains for Nonfullerene Solar Cells. *J. Org. Chem.* **2017**, *82*, 5926−5931.
(34) Roy, R.; Khan, A.; Chatterjee, O.; Bhunia, S.; Koner, A. L. Perylene Monoimide as a Versatile Fluoroprobe: The Past, Present, and Future. *Org. Mater.* **2021**, *3*, 417−454.
(35) Cardona, C. M.; Li, W.; Kaifer, A. E.; Stockdale, D.; Bazan, G. C. Electrochemical considerations for determining absolute frontier orbital energy levels of conjugated polymers for solar cell applications. *Adv. Mater.* **2011**, *23*, 2367−2371.
(36) Bertrandie, J.; Han, J.; de Castro, C. S. P.; Yengel, E.; Gorenflot, J.; Anthopoulos, T.; Laquai, F.; Sharma, A.; Baran, D. The Energy Level Conundrum of Organic Semiconductors in Solar Cells. *Adv. Mater.* **2022**, *34*, 2202575.
(37) Bredas, J.-L. Mind the gap! *Mater. Horiz.* **2014**, *1*, 17−19.
(38) Knall, A.-C.; Hoefler, S. F.; Hollauf, M.; Thaler, F.; Noesberger, S.; Hanzu, I.; Ehmann, H.; Hobisch, M.; Spirk, S.; Wen, S.; Yang, R.; Rath, T.; Trimmel, G. Synthesis of a tetrazine-quaterthiophene copolymer and its optical, structural and photovoltaic properties. *J. Mater. Sci.* **2019**, *54*, 10065−10076.
(39) Owens, D. K.; Wendt, R. C. Estimation of the surface free energy of polymers. *J. Appl. Polym. Sci.* **1969**, *13*, 1741−1747.
(40) Wu, S. Calculation of interfacial tension in polymer systems. *J. Polym. Sci., Part C: Polym. Symp.* **1971**, *34*, 19−30.
(41) Sun, C.; Pan, F.; Bin, H.; Zhang, J.; Xue, L.; Qiu, B.; Wei, Z.; Zhang, Z.-G.; Li, Y. A low cost and high performance polymer donor material for polymer solar cells. *Nat. Commun.* **2018**, *9*, 743.
(42) Alfonsi, K.; Colberg, J.; Dunn, P. J.; Fevig, T.; Jennings, S.; Johnson, T. A.; Kleine, H. P.; Knight, C.; Nagy, M. A.; Perry, D. A.; Stefaniak, M. Green chemistry tools to influence a medicinal chemistry and research chemistry based organisation. *Green Chem.* **2008**, *10*, 31−36.
(43) Sartorius Stedim Data Analytics AB. *MODDE Pro (Version 13.0.2.34314)*; Sartorius Stedim Data Analytics AB: Umea, Sweden, 2021.
(44) Dong, S.; Zhang, K.; Xie, B.; Xiao, J.; Yip, H.-L.; Yan, H.; Huang, F.; Cao, Y. High-Performance Large-Area Organic Solar Cells Enabled by Sequential Bilayer Processing via Nonhalogenated Solvents. *Adv. Energy Mater.* **2019**, *9*, 1802832.
(45) Yang, B.; Yuan, Y.; Huang, J. Reduced Bimolecular Charge Recombination Loss in Thermally Annealed Bilayer Heterojunction Photovoltaic Devices with Large External Quantum Efficiency and Fill Factor. *J. Phys. Chem. C* **2014**, *118*, 5196−5202.
(46) Cheknane, A.; Hilal, H. S.; Djeffal, F.; Benyoucef, B.; Charles, J.-P. An equivalent circuit approach to organic solar cell modelling. *Microelectron. J.* **2008**, *39*, 1173−1180.
(47) Koster, L. J. A.; Mihailetchi, v. d.; Xie, H.; Blom, P. W. M. Origin of the light intensity dependence of the short-circuit current of polymer/fullerene solar cells. *Appl. Phys. Lett.* **2005**, *87*, 203502.
(48) Koster, L. J. A.; Mihailetchi, v. d.; Ramaker, R.; Blom, P. W. M. Light intensity dependence of open-circuit voltage of polymer:-fullerene solar cells. *Appl. Phys. Lett.* **2005**, *86*, 123509.
(49) Strasser, S.; Slugovc, C. Nucleophile-mediated oxa-Michael addition reactions of divinyl sulfone − a thiol-free option for step-growth polymerisations. *Catal. Sci. Technol.* **2015**, *5*, 5091−5094.
(50) Nomiyama, S.; Ogura, T.; Ishida, H.; Aoki, K.; Tsuchimoto, T. Indium-Catalyzed Regioselective β-Alkylation of Pyrroles with Carbonyl Compounds and Hydrosilanes and Its Application to Construction of a Quaternary Carbon Center with a β-Pyrrolyl Group. *J. Org. Chem.* **2017**, *82*, 5178−5197.

https://doi.org/10.1021/acsaem.2c03433
ACS Appl. Energy Mater. 2023, 6, 1544−1554